



Promotion effects of potassium on the activity and selectivity of Pt/zeolite catalysts for reverse water gas shift reaction



Xiaoli Yang^{a,b,1}, Xiong Su^{a,1}, Xiaodong Chen^{a,b}, Hongmin Duan^a, Binglian Liang^{a,b}, Qinggang Liu^a, Xiaoyan Liu^a, Yujing Ren^{a,b}, Yanqiang Huang^{a,*}, Tao Zhang^a

^a State Key Laboratory of Catalysis, Dalian Institute of Chemical Physics, Chinese Academy of Sciences, No. 457 Zhongshan Road, Dalian 116023, PR China

^b University of Chinese Academy of Sciences, Beijing 100049, PR China

ARTICLE INFO

Article history:

Received 2 March 2017

Received in revised form 9 May 2017

Accepted 22 May 2017

Available online 24 May 2017

Keywords:

RWGS

KTTL zeolite

Potassium promoter

Formate

ABSTRACT

Catalytic hydrogenation of carbon dioxide to CO by reverse water gas shift reaction plays a vital role in the recycling of the abundant carbon source. Here, the reaction over a series of zeolite L-supported platinum catalysts was systematically investigated to study the promoting role of potassium. The results of activity tests showed that controlled addition of potassium promoter to Pt/L catalyst was beneficial for the catalytic activity and selectivity. It was observed that cage encapsulation by zeolite pores could stabilize Pt nano-particles even at severe reaction conditions. Furthermore, X-ray absorption near edge structure and X-ray photoelectron spectra results demonstrated that the chemical state of platinum was altered by the additional potassium promoter, providing evidence for the formation of Pt-O(OH)-K interfacial sites. Thereafter, the Pt-O(OH)-K interfaces, acting as main active sites to adsorb CO₂ and produce bridge-bonded formate intermediates, were identified by a set of *in-situ* diffuse reflectance Fourier transform infrared spectroscopy and microcalorimetry measurements. This finding provides new insights into the use of a variety of zeolite as carriers for highly dispersed noble metal in catalytic CO₂ reduction.

© 2017 Elsevier B.V. All rights reserved.

1. Introduction

Recently, the massive anthropologic emissions of carbon dioxide have become a major global issue, which has triggered severe climate change and ocean acidification. In order to reduce the atmospheric CO₂ content [1–3], great efforts have been dedicated to the transitioning of CO₂ into chemicals or fuels, as CO₂ can be served as a cheap, non-toxic, and colossal carbon resource reservoir [4]. Among the most widely attainable approaches to the recycling of CO₂, catalytic conversion of CO₂ to CO, also known as the reverse water-gas shift (RWGS) reaction, has the highest potential efficiency. Firstly, it is regarded to be the key intermediate step for many vital CO₂ hydrogenation processes [5,6], such as Sabatier reaction and methanol synthesis [7], thus being considered as the building block stage. Furthermore, the formation of CO gives an additional versatility in the successive use because CO could be transformed to a variety of energy-rich commodities, which is of great importance to the development of long term fossil-C indus-

try. For instance, Hu et al. have reported the hydrogenation of CO₂ to light olefins, which was associated with RWGS process and then followed by Fischer-Tropsch reaction (FTO) [8]. In addition, the RWGS reaction is also important for the outer space exploration owing to the high CO₂ levels on Mars and accumulated within the closed life cycle in spaceship. The generation of H₂, as a coproduct of oxygen generation from water splitting, makes this process more reliable. Therefore, RWGS reaction is a promising process with a wide variety of potential end uses.



Notably, RWGS reaction is thermodynamically favorable at high temperature because of its endothermic nature [9], as shown in equation (1). However, an additional side reaction, the Sabatier reaction, would occur under similar reaction conditions, making it difficult to achieve with high selectivity. In recent years, considerable research works have been dedicated to improve the RWGS selectivity by elucidating the reaction mechanism [10–12] and acquiring desired catalyst structure with tunable metal particle size [13–15], support types [16,17], and promoters [18–20]. Researchers have identified that the reduction in metal particle size can significantly increase the selectivity of CO [21,22]. In an attempt to promote the activity and selectivity simultaneously,

* Corresponding author.

E-mail addresses: yqhuang@dicp.ac.cn, yqhuangdicp@gmail.com (Y. Huang).

¹ These authors contributed equally to this work.

deep insights into the structure correlated catalytic performance in RWGS are still needed. Namely, both facile CO_2 activation from $\text{C}=\text{O}$ bond scission and efficient CO desorption are worthy being considered when synthesizing well-performed catalysts [23].

As RWGS is the reverse process of water gas shift (WGS) reaction, cognitions on the well-developed WGS catalysts are inherently beneficial for RWGS reaction. For instance, Flytzani-Stephanopoulos and co-workers have synthesized a series of catalysts containing $\text{M}-\text{O}(\text{OH})_x$ ensembles and found that these species not only promoted the stability of metal particles but also facilitated to catalyze low temperature WGS reaction [24–26], which may also be feasible for RWGS reaction. Indeed, attempts have been successfully implemented in the use of reducible oxides as supports, such as ceria, titania, etc., which may acquire high activities [27]. However, the supported metals suffer from severe sintering due to the unstable nature of reducible oxides as exposed to high reaction temperature. Hence, these kinds of catalysts can hardly guarantee high activity and selectivity simultaneously. Another approach is creating $\text{M}-\text{O}(\text{OH})_x$ linkage by adding alkali metal to “inert” oxide supports such as zeolites or silica [28]. The resultant catalysts have comparable activity but also improved stability as compared to reducible oxide supported catalysts [29]. Specially, zeolites have well developed pore structures and good thermal stability, making them widely applied as catalysts and carriers. A number of recent studies have elucidated the encapsulation of single-atoms or metal clusters into zeolite pores with highly thermal stability [30]. Different from other reactions, the alkalis promoters also facilitate the adsorption of acidic CO_2 owing the basic nature during the RWGS reaction [31]. The creation of $\text{M}-\text{O}(\text{OH})_x-\text{Na}(\text{K})$ entities in zeolites may thus provide stable avenues for RWGS reaction.

In this work, KLTL (L) zeolite was firstly employed as the support of Pt catalyst for catalyzing RWGS reaction. Besides, as the promoter, different contents of KOH were added to Pt/L catalyst to make a comparison, which exhibited a varied activity and selectivity. In an effort to understand the effect of potassium promoter, multi-techniques were employed to examine the structural and electronic properties of $\text{K}_x\text{-Pt}/\text{zeolite}$ catalysts thoroughly. In addition, the active sites and the intermediates during the RWGS process were also detected, contributing to reveal the intermediates for RWGS reaction.

2. Experimental section

2.1. Materials

Pseudo-boehmite and silica sol were purchased from Tianjin Kemiou Chemical Reagent Co., Ltd. (Tianjin, China). Potassium hydroxide and $\text{Pt}(\text{NH}_3)_4(\text{NO}_3)_2$ were purchased from Sigma-Aldrich Co. LLC. All chemicals were used as received without further purification.

2.2. Catalyst preparation

2.2.1. Preparation of parent zeolite KLTL

Scheme 1 shows the general procedures for the synthesis of zeolite associated samples. Parent zeolite L was synthesized by a hydrothermal method as reported previously [32]. In a typical synthesis, potassium hydroxide, pseudo-boehmite, silica-sol and water, with the molar ratio of $10\text{K}_2\text{O}:20\text{SiO}_2:\text{Al}_2\text{O}_3:400\text{H}_2\text{O}$, were added in sequence into a glass beaker. The mixture was stirred at room temperature for 1 h and then transferred to a 100 ml stainless-steel autoclave, tightly sealed. The autoclave was then heated in a forced convection oven with rotation (30 rpm) at 175 °C for 8 h. After crystallization, the resulting solid was recovered by centrifu-

gation, washed with deionized water and dried at 80 °C overnight, followed by calcination in air at 550 °C to obtain the final product.

2.2.2. Preparation of $\text{K}_x\text{-Pt/L}$ catalysts

Pt/zeolite sample with a metal content of 0.3 wt.% (determined by inductively coupled plasma measurement) was prepared by ion exchange using $\text{Pt}(\text{NH}_3)_4(\text{NO}_3)_2$ as the precursor. Typically, a suspension containing 1 g parent zeolite L and 180 ml deionized water was stirred at 30 °C for 30 min. An aqueous solution (20 ml) of $\text{Pt}(\text{NH}_3)_4(\text{NO}_3)_2$ (0.025 wt.% $\text{Pt}(\text{NH}_3)_4(\text{NO}_3)_2$ in ultrapure water) was added dropwise into the slurry with vigorous stirring. After recovered by filtration and washing, the obtained solid product was dried in dark vacuum at RT overnight. Meanwhile, a commercial H-ZSM-5 ($\text{SiO}_2/\text{Al}_2\text{O}_3 = 50$, purchased from Nankai University Catalyst Co.) was employed to synthesize the catalyst with acidic zeolite as carrier. To ensure the same amount of Pt loading, a higher concentration of precursor (0.05 wt.% $\text{Pt}(\text{NH}_3)_4(\text{NO}_3)_2$) was used because of the relatively lower ion exchange rate. The catalysts thus harvested were denoted as Pt/L and Pt/ZSM-5, respectively.

Potassium was introduced into the catalysts by means of a solid-state impregnation (SSI) method. The dry Pt/L catalysts and required amount of KOH powder were ground together under N_2 protection for 30 min. The mixture was dried in dark vacuum at RT overnight. The resulting samples were denoted as $\text{K}_x\text{-Pt/L}$, where x represents the K/Pt atomic ratio. All catalysts were pre-reduced at 500 °C in pure H_2 flow before using.

2.3. Activity measurements

RWGS measurements were carried out in a continuous flow fixed-bed reactor (i.d. 10 mm) under atmospheric pressure. The reaction temperature was measured and controlled with a K-type thermocouple that was located at the central axis of the catalyst bed. All gas flows were controlled by mass flow controllers. The composition of feed gas was as follows: 45 vol.% CO_2 , 45 vol.% H_2 and balanced with 10 vol.% N_2 (also employed as calibrating gas). Prior to the activity tests, 100 mg of catalyst ($\text{dp} = 20\text{--}40$ mesh) was pre-reduced under the feed gas flow (50 ml min⁻¹, STP) at 500 °C for 1 h. The catalytic activity was measured in the temperature range of 200–500 °C with a constant gas flow rate of 50 ml min⁻¹, corresponding to 30000 ml g_{cat}⁻¹ h⁻¹. The effluent gas product was allowed to pass through an ice-bath unit to remove the water vapor and then analyzed online by gas chromatography (Agilent 6890N equipped with TDX-01 column and TCD detector).

The CO_2 conversion was calculated as follows,

$$\text{Conversion}(\text{CO}_2\%) = \frac{\text{CO}_2(\text{in}) - \text{CO}_2(\text{out}) \times \frac{\text{N}_2(\text{in})}{\text{N}_2(\text{out})}}{\text{CO}_2(\text{in})} \times 100\%$$

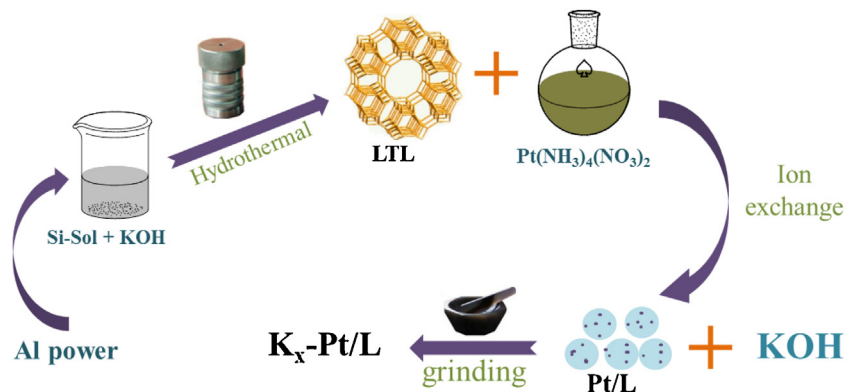
Where $\text{CO}_2(\text{in})$ and $\text{N}_2(\text{in})$ represent the CO_2 and N_2 concentrations at the inlet, $\text{CO}_2(\text{out})$ and $\text{N}_2(\text{out})$ correspond to the CO_2 and N_2 concentrations at the outlet, respectively.

Based on the conversion of CO_2 , the reaction rate was calculated using the following expression,

$$r = \frac{x \times F_{\text{CO}_2}}{M}$$

Where r is the reaction rate of CO_2 (mol g_{cat}⁻¹ h⁻¹), F_{CO_2} is the flow rate (mol h⁻¹), M is the mass of catalyst (g), and x is the conversion of CO_2 . Additionally, the Pt dispersion is determined by assessing the portion of surface exposed atoms from the average particle diameter with STEM images [33].

$$D = \frac{1.13}{d}$$



Scheme 1. Synthesis procedures of K_x -Pt/L catalysts.

Where D is the metal dispersion; d is the diameter of Pt particles (nm).

The turnover frequency (TOF) of CO_2 is calculated depending on the metal dispersion, which is defined as the moles of CO_2 converted per mole surface metal atom per second (s^{-1}),

$$TOF = \frac{r \times M_{Pt}}{D \times x}$$

Where M_{Pt} corresponds to the atomic weight; x is the metal content ($g_{met} g_{cat}^{-1}$). The TOF values over all catalysts here were calculated based on the CO_2 conversion at $400^\circ C$, which were controlled below 15%.

2.4. Characterizations

The Pt contents were determined by inductively coupled plasma optical emission spectrometer (ICP-OES) on an IRIS Intrepid II XSP instrument. Catalyst morphologies were observed on a JSM-7800F scanning electron microscopy (SEM). The specific surface area of the catalysts was determined from N_2 physical adsorption-desorption isotherms on an ASAP 2460 Quantachrome instrument, and calculated by BET (Brunauer-Emmett-Teller) equation. Before analysis, the samples were degassed at $300^\circ C$ in vacuum for 6 h. Powder X-ray diffraction (XRD) patterns were collected on a PW3040/60 X' Pert ProSuper (PANalytical) diffract meter using $Cu K\alpha$ radiation source ($\lambda = 0.15432\text{ nm}$, 40 kV , 40 mA). Measurements were carried out in the 2θ range between 5° and 50° , with a scanning speed of 4° min^{-1} . The morphology and size of metal particles were observed by high-angle annular dark-field scanning transmission electron microscopy (HAADF-STEM) using a JEM-2100F instrument at 200 kV . The particle size distributions of all catalysts were obtained by measuring more than 500 particles from 10 individual spots randomly to ensure the accuracy of the data. X-ray photoelectron spectra (XPS) were determined on a VG ESCALAB 210 apparatus using $Al K\alpha$ ($h\nu = 1486.6\text{ eV}$) as the X-ray source. Since zeolite L contains large amounts of aluminum, of which the $2p$ energy region is approximately identical to $Pt 4f_{7/2}$ [34], the core-level spectra of $Pt 4d_{5/2}$ were collected. Spectra were referenced to the valence band of $Si 2p$ peak at 103 eV binding energy (BE). The samples were prerduced at $500^\circ C$ before the measurements.

Temperature programmed reduction (TPR) measurements were performed on a micromeritics AutoChem II 2920 apparatus. Typically, the samples were pretreated with Ar at $150^\circ C$ for 60 min. After cooling to $50^\circ C$, 10 vol.% H_2/Ar was allowed to pass through the catalyst bed and then heated to $500^\circ C$ with a ramping rate of $10^\circ C \text{ min}^{-1}$. X-ray absorption near edge structure (XANES) at Pt LIII-edge of the samples was measured at the beamline 14W of Shanghai Synchrotron Radiation Facility (SSRF) in China. The output beam was selected by $Si (311)$ monochromator with a

Pt foil employed for energy calibration. Before measurements, the samples were all reduced at $500^\circ C$ and sealed with Kapton film in a glove box. The data were collected at room temperature under fluorescence mode by using solid state detector. Athena software package was employed to process the XANES data. Fourier-transform infrared (FTIR) spectra were collected on a Bruker EQUINOX-55 infrared spectrometer equipped with a DTGS detector. Prior to CO chemisorption, samples were pretreated under H_2 flow (20 ml min^{-1}) at $500^\circ C$ for 1 h, followed by evacuation at the same temperature for 0.5 h. After cooling to $50^\circ C$, a background spectrum was collected, and subtracted automatically from the measured spectra. The reduced catalysts were then exposed to 1 vol.% CO/He until the CO signals unchanged. The system was purged with He to remove the gaseous CO and the signals were collected. Meanwhile, *in-situ* diffuse reflectance Fourier transform infrared spectroscopy (DRIFT) was also performed at $150^\circ C$ under the pure feed gas flow (5 ml min^{-1}) after the above-mentioned pretreatment process.

Heats of CO_2 adsorption were measured at $40^\circ C$ with a BT 2.15 heat-flux calorimeter connected to a gas handling and a volumetric system equipped with MKS 698A baratron capacitance manometers ($\pm 1.33 \times 10^{-2}\text{ Pa}$). Prior to each adsorption, the samples were pre-reduced at $500^\circ C$ for 1 h and evacuated for 0.5 h, and then cooled to room temperature in *vacuo*. Subsequently, the quartz tube was refilled with He and tightly sealed. After the pretreatment, the samples were outgassed at $40^\circ C$ overnight in the calorimetric cell, which was immersed within the isothermal calorimetric block to ensure that the residual pressure fell below 3×10^{-3} torr. The adsorption of CO_2 was done with point by point introduction of pure CO_2 up to a pressure of ~ 10 Torr at $40^\circ C$.

3. Results and discussion

3.1. Catalytic properties

Fig. 1 displays the catalytic performance of RWGS reaction and the corresponding calculated Arrhenius plots over these Pt/zeolite catalysts. In all cases, CO_2 conversion (panel a) increased monotonically as the reaction temperature elevated. It is worth noting that distinct difference in catalytic activity was observed on the catalysts with different potassium content. $Pt/ZSM-5$, a K-free catalyst with the acidic ZSM-5 zeolite as support, exhibited extremely poor activity during the entire reaction temperature range. On the contrary, Pt/L showed much improved catalytic performance owing to the basicity of K in zeolite L support. The CO_2 conversion was only 0.9% at $325^\circ C$ and increased to 13.1% at $500^\circ C$. As the additional K content increases (i.e., from 0 to K_{80}), the CO_2 conversion increased significantly from 13.1% to 27.4% when reacted at $500^\circ C$.

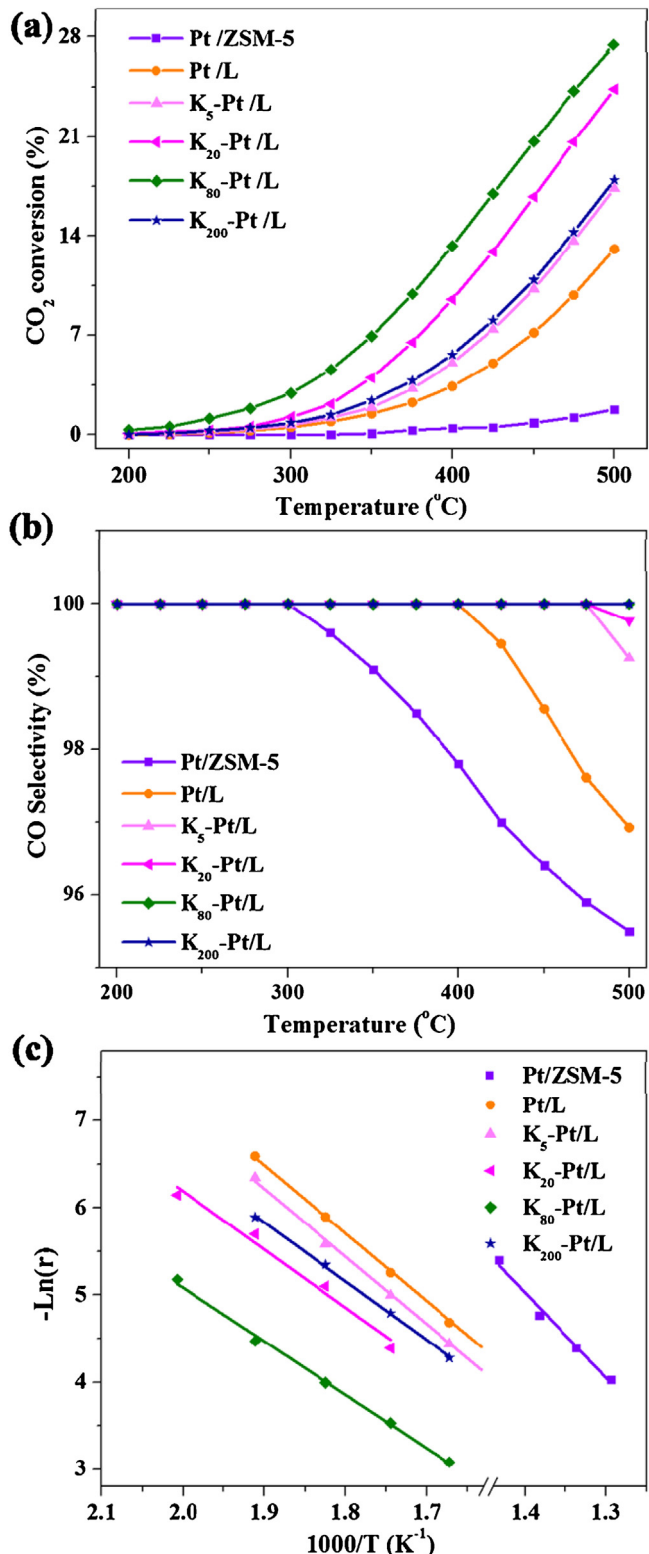


Fig. 1. (a) CO₂ conversion and (b) CO selectivity as a function of reaction temperature; (c) Arrhenius plots of CO₂ hydrogenation over the catalysts with different K contents. Reaction conditions: 0.1 MPa, H₂/CO₂/N₂ = 45/45/10 (v/v/v), GHSV is 30000 ml_{STP} g⁻¹ h⁻¹.

Further increasing the K amount to K₂₀₀ led to a decrease in the conversion of CO₂ to 17.9%. Surprisingly, unlike other catalysts with oxides as substrate, methane product was almost undetectable in our cases. The selectivity of CO on the series of K_x-Pt/L catalysts was higher than 95% (Fig. 1b). Additionally, there existed a slight increasing trend in the selectivity with the potassium content, illustrating that potassium promoter favored the improvement of the reaction selectivity.

Not surprisingly, in consistent with the CO₂ conversion, the determined TOF values followed the same trend as the additional amount of K, with a maximum value of 2.25 s⁻¹ over K₈₀-Pt/L. It is interesting to notice that the TOF values over these K_x-Pt/L catalysts are higher than the comparative data that happened over most of other catalysts [35,36], which were summarized in Table S2. These results showed that catalysts with alkali metal promoted zeolite as substrate could catalyze the conversion of CO₂ with high efficiency.

Table 1 also summarizes the apparent activation energy (E_a) of CO₂ hydrogenation over these catalysts. As demonstrated in Fig. 1(c), each line shows reasonable linearity in the reaction temperature regime. The E_a value over Pt/ZSM-5 was 80 ± 5.1 kJ mol⁻¹, much higher than that over K_x-Pt/L catalysts (50–60 kJ mol⁻¹). This notable discrepancy between Pt/ZSM-5 and K_x-Pt/L implies that there exists great difference in the activation barriers and further in the reaction pathways. On the other hand, the similar E_a values over the series K_x-Pt/L catalysts indicate the same reaction path but different in the distribution of active sites.

It is clear that a certain amount of K can greatly promote the activity of RWGS reaction, whereas too much addition plays a counterproductive impact. In order to investigate the influence of K promoter and figure out the active sites, the structural and electronic properties of K_x-Pt/L catalysts were thoroughly characterized.

3.2. Catalyst characterizations

3.2.1. The influence of potassium on the catalyst structure

SEM, XRD, and N₂ physical sorption were performed to assess the impact of additive K promoter upon the structure of these Pt/zeolite catalysts. Fig. 2 shows the morphologies of these catalysts with different amount of K addition. Obviously, only Pt/L shows identical structure with parent zeolite L. However, for K_x-Pt/L, the apparent structure of carrier was damaged to different extents along with the increased amount of K promoter. Small pieces of fragments appeared around zeolite, which might be either broken zeolite species or the potassium component, especially in K₂₀₀-Pt/L.

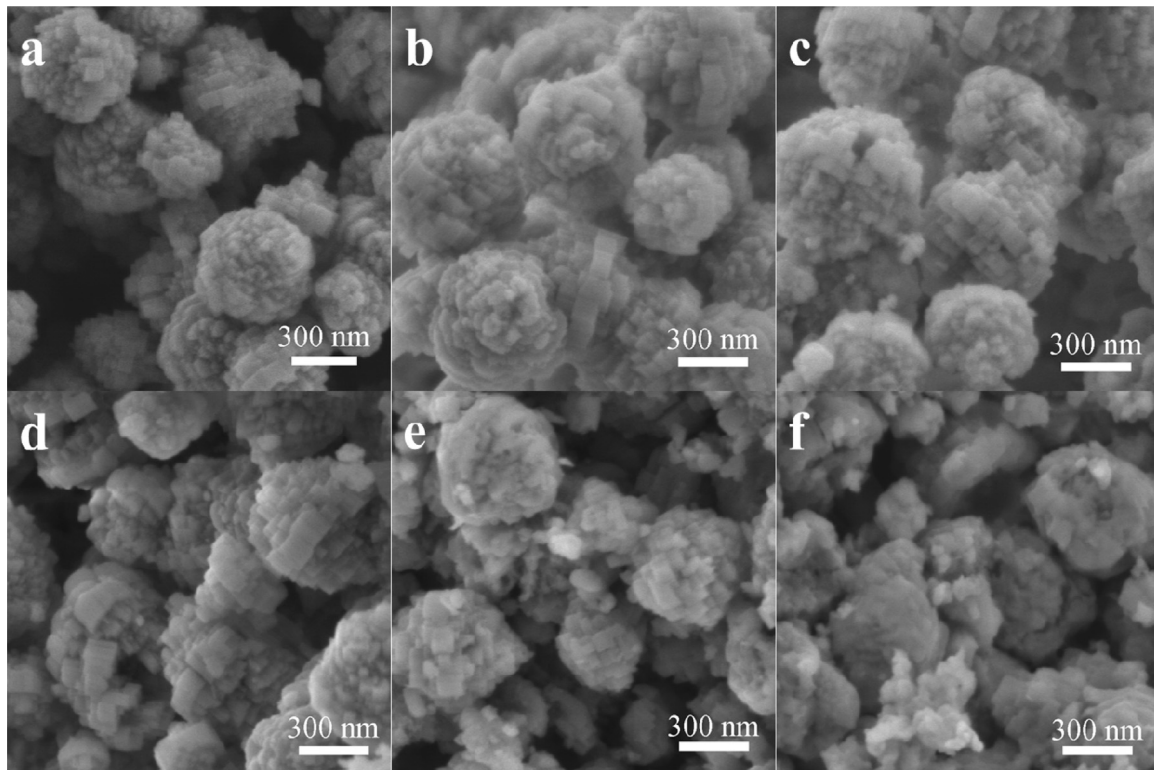
The specific BET surface area and pore distribution properties were collected from N₂ physical adsorption to further estimate the varieties in the support structure, which are summarized in Table 2. With the increased content of K promoter, the surface area and micropore volume decreased rapidly, indicating that parts of the particles were broken or a large portion of micropore was blocked by the K component. Specially, the micropore structure in K₂₀₀-Pt/L could not be detected.

The structural changes of K_x-Pt/L catalysts caused by the addition of KOH were also analyzed through XRD patterns, as displayed in Fig. 3. Notably, Pt/L showed little change as compared with parent zeolite L (see Fig. S1). However, the relative crystallinity of the support in K_x-Pt/L reduced rapidly with the increase of K content, especially for the peak at $2\theta = 5.6^\circ$, which was in accordance with the observation from SEM images. In all these catalysts (fresh or used), no reflection of metallic Pt was detected, indicating that Pt particles with small size were primarily included. The absence of bulk Pt metal peaks even after a high temperature treatment at 500 °C reflected the excellent stability of Pt particles. Also, no potassium species were observable under the K content of K₈₀, implying

Table 1

The chemical parameters for Pt/zeolite catalysts with different potassium contents.

Samples	Pt dispersion /%	Reaction rate /mol g _{cat} ⁻¹ h ⁻¹	TOF /s ⁻¹	E_a /kJ mol ⁻¹
Pt/ZSM-5	56.6	0.003	0.10	80±5.2
Pt/L	80.9	0.021	0.53	60±1.2
K ₅ -Pt/L	87.1	0.030	0.61	57±1.3
K ₂₀ -Pt/L	70.8	0.057	1.52	55±4.5
K ₈₀ -Pt/L	66.6	0.080	2.25	50±1.5
K ₂₀₀ -Pt/L	41.9	0.034	1.47	56±1.1

**Fig. 2.** SEM images of K_x-Pt/L catalysts with different K contents: (a) parent L; (b) Pt/L; (c) K₅-Pt/L; (d) K₂₀-Pt/L; (e) K₈₀-Pt/L and (f) K₂₀₀-Pt/L.**Table 2**BET surface areas and pore volumes of K_x-Pt/L samples.

Samples	S _{BET} /m ² g ⁻¹	S _{micro} /m ² g ⁻¹	S _{meso} /m ² g ⁻¹	V _{micro} /cm ³ g ⁻¹	V _{meso} /cm ³ g ⁻¹	Medium pore width /nm
L	335	252	83	0.10	0.10	0.57
Pt/L	329	247	82	0.10	0.10	0.58
K ₅ -Pt/L	308	222	86	0.10	0.11	0.58
K ₂₀ -Pt/L	212	139	73	0.06	0.09	0.59
K ₈₀ -Pt/L	72	19	52	0.01	0.07	0.73
K ₂₀₀ -Pt/L	11	– ^a	– ^a	– ^a	– ^a	0.97

^a Not determined.

the high dispersion of potassium component [37]. Nevertheless, five new peaks at $2\theta = 12.8^\circ$, 29.7° , 32.2° , 32.6° and 40.5° , corresponding to potassium carbonate, were detected over K₂₀₀-Pt/L. In other words, potassium could not be dispersed uniformly in zeolite when the additive amount was too high, and potassium carbonate appeared owing to the easily adsorption of CO₂ with large amount of alkaline precursors.

3.2.2. The metal particles size

It was reported that the metal particle size is significant for the catalytic activity and selectivity of RWGS reaction [38,39]. HAADF-STEM images of these Pt/zeolite catalysts were thus collected. As shown in Fig. 4, Pt metal particles could maintain high dispersion even after reduction at 500 °C (with the mean particle size

of ~ 1.5 nm), except for the K₂₀₀-Pt/L sample (enlarged to ~ 2.7 nm). In the report of Wu et al. [40], the encapsulated noble metal clusters within LTA zeolite voids showed remarkable resistance against thermal sintering because of the confinement effect. Yang and co-workers also summarized that physical encapsulation by zeolite was an efficient strategy in the stabilization of metal particles even at elevated temperature [41]. In our study, the stabilized nanoparticles with mean particle size of less than 2 nm might benefit from the same origin. However, as the particles of K₂₀₀-Pt/L were damaged with too much K addition, the statistical mean size of Pt particles in K₂₀₀-Pt/L was much larger than that over other catalysts. Consequently, the weakened encapsulation role and uneven distribution of metal particles possibly led to the poor catalytic performance in RWGS reaction. From another perspective, statistical compar-

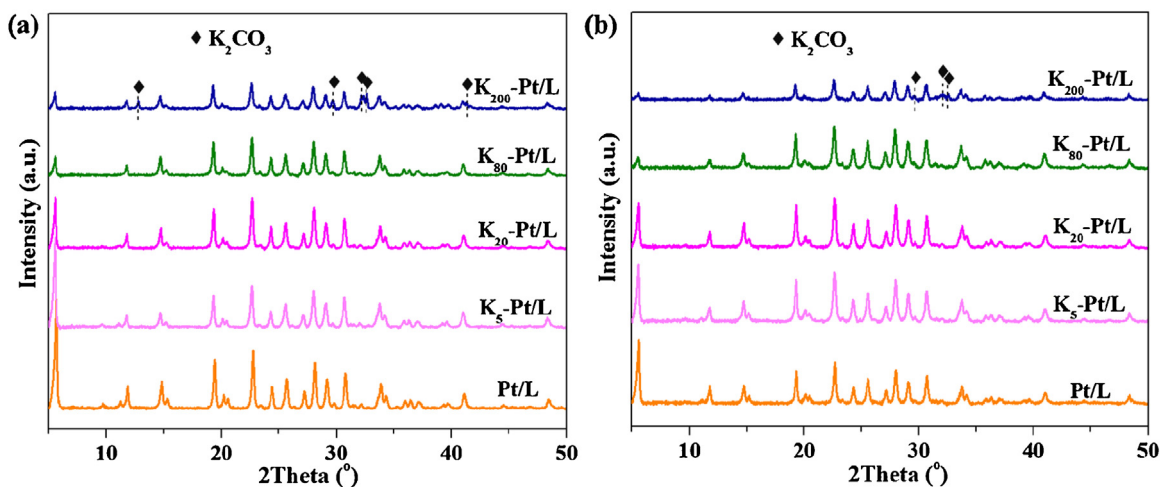


Fig. 3. XRD patterns of K_x -Pt/L catalysts with different K contents: (a) collected before reaction and (b) collected after reaction. \blacklozenge represents the K_2CO_3 species.

ions also revealed that the metal particles over Pt/ZSM-5 (with a mean value of 2.0 nm) were less uniformly dispersed than that over K_x -Pt/L, indicating that potassium species might promote the stabilization of Pt particles [42].

To further figure out the detailed metal particle distribution in K_{80} -Pt/L, aberration-corrected transmission electron microscope was employed (Fig. 5). As expected, no large particles emerged in the image with large visual field, verifying the high dispersion of Pt particles. The focus region was also acquired in an amplified vision to observe more specific features. Surprisingly, we found that a few Pt particles were separated into tiny clusters and overlaid by some substances. It illustrated that an interface was formed between the Pt particle surface and the substance, which most likely to be the additive potassium species.

3.2.3. Chemical state of Pt

H_2 temperature-programmed reduction (H_2 -TPR) measurements over these K_x -Pt/L catalysts were carried out to elucidate the influence of additive K on the chemical state of Pt particles [43–45]. The first peak, corresponding to the reduction of PtO_x , shifted to a high temperature region when more additive potassium was added, see Fig. 6(a). As described previously, Zhu [46] and Liang [47] et al. had mentioned the strong interaction between metal and alkaline promoters. Similarly in our cases, the additive K species might separate or overlay Pt particles, thus generating strong interaction at their interfaces and hindering the reduction degree of PtO_x species. In an effort to identify if there was charge transfer between Pt and K promoters, Pt LIII-edge XANES spectra of Pt/ZSM-5, Pt/L and K_{10} -Pt/L catalysts were measured, see Fig. 6(b). The white-line of these catalysts became intensified and shifted to a higher energy region with the increase of K content, accounting for the high oxidation state of Pt. Therefore, a charge transfer occurred at the interface sites. A similar observation on the interaction between K and Pt had been reported on the study of Pt-O(OH)-K system [42].

The alteration in the chemical state of surface Pt species with the addition of K was also investigated by XPS analysis, as displayed in Fig. 6(c). Clearly, the areas of these signals decreased gradually because of the lowered degree of exposure on the Pt particle surface. The signal of K_{200} -Pt/L could even not be collected, indicating the inaccessibility of Pt particles, which in turn caused low RWGS activity. On the other hand, it could be deduced that the interface between Pt and K species might result in electron transfer through the linkage of Pt-O(OH)-K. Therefore, the broad peak was deconvoluted into two peaks in the $Pt4d_{5/2}$ region, corresponding to $Pt^{\delta+}$

at 317.6 eV and metallic Pt^0 at 315.3 eV, respectively [48]. Furthermore, it was noted that the ratio of $Pt^{\delta+}/Pt^0$ increased with the increase of potassium loading from the curve-fitting data, as listed in Table 3.

Fig. 7 shows the FTIR spectra via CO adsorption to further probe the distribution and chemical state of Pt species. All the signals are tailing-like, which can be fitted into two peaks. The intense peak situated at $\nu = 2076\text{ cm}^{-1}$ was attributed to linear-bonded CO on metallic Pt [49]. The other peak at $\nu = 2010\text{ cm}^{-1}$ was ascribed to CO adsorbed at the interface between platinum and K promoter [50–53]. There is a distinct broad CO adsorption peak on Pt/L and K_5 -Pt/L between 2010 cm^{-1} and 2076 cm^{-1} , but the intensity tended to decrease with the increased amount of additive K. We further focused on the relative intensity of the two signals, which showed an increased trend of CO adsorption on the interfacial sites. Therefore, the data presented here substantially demonstrated the coverage of Pt surfaces but with increased appearance of interfaces owing to the addition of K promoter.

Based on the above discussions, the addition of potassium promoter overlaid Pt particles and created Pt-O(OH)-K interface sites where the work function of Pt was increased [54,55]. As a consequence, the adsorption properties of H_2 and CO were changed, which might be the reason of promoted catalytic performance in RWGS reaction. In an attempt to figure out the reaction pathway over these active sites, more characterizations based on the dynamic adsorption/desorption behaviors were adopted.

3.3. The active sites and intermediates

In order to evaluate if Pt-O(OH)-K species were also active sites to catalyze RWGS reaction, microcalorimetry which exquisitely provides information on the enthalpy of CO_2 adsorption was carried out [56,57]. As seen in Fig. 8(a), the initial rapid adsorption stage of CO_2 in the lower pressure range (less than 0.5 Torr) was assigned as chemisorption. Then, the increased trends of adsorption became gentle gradually, which was assigned as physical adsorption. The slopes owing to the physical adsorption decreased with the increase of K content, confirming that the zeolite voids were filled by potassium species. Fig. 8(b) shows the heats of adsorption as a function of CO_2 coverage on the catalyst surface. For the K_x -Pt/L ($x = 20, 80, 200$) samples, the initial heats of CO_2 adsorption were about 115 kJ mol^{-1} , much higher than that over the other two catalysts (approximately 90 kJ mol^{-1}), indicating a stronger interaction between CO_2 and the former one [58]. The adsorption sites could

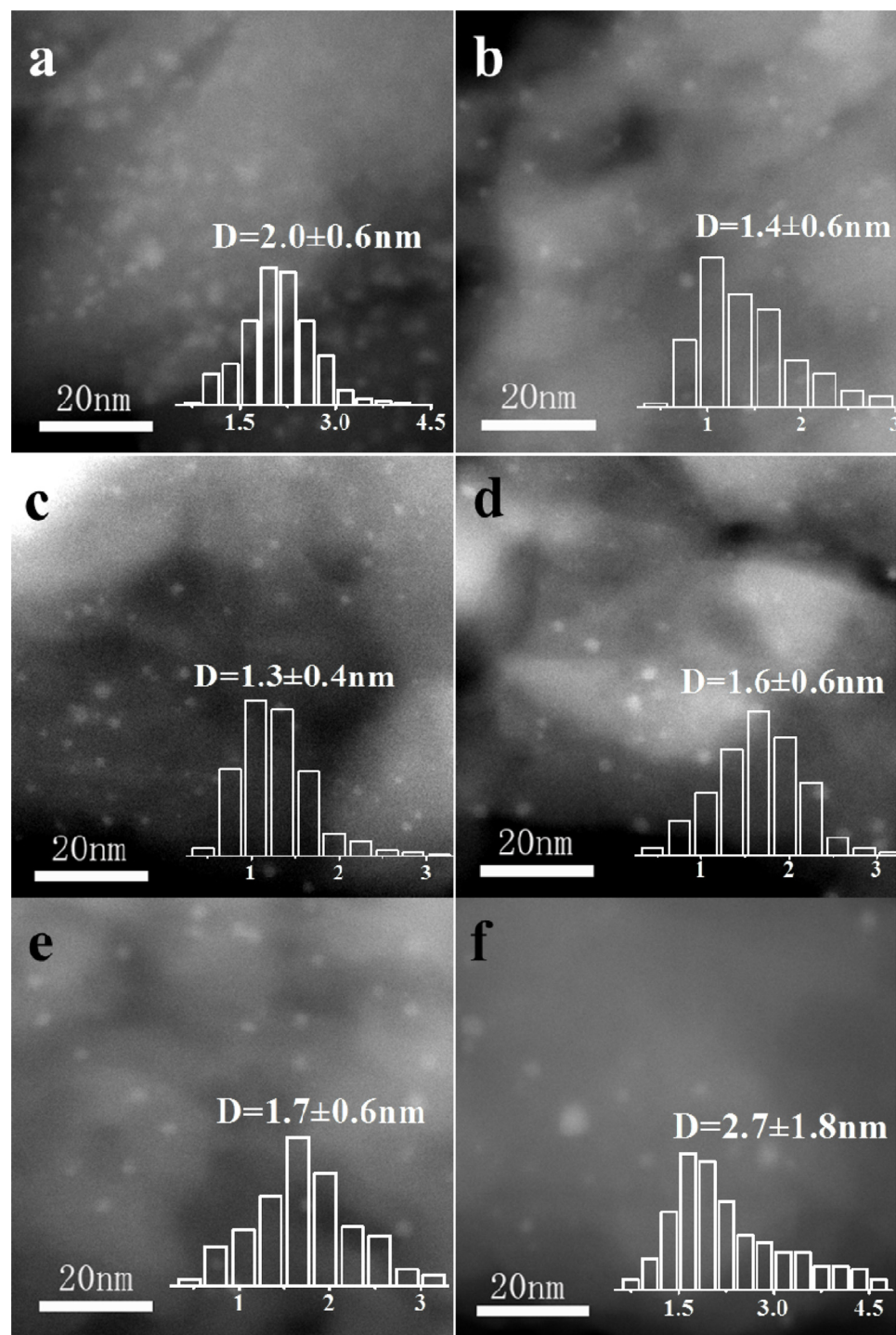


Fig. 4. HAADF-STEM images of Pt/zeolite catalysts and the corresponding statistical particle size distributions: (a) Pt/ZSM-5; (b) Pt/L; (c) K₅-Pt/L; (d), K₂₀-Pt/L; (e) K₈₀-Pt/L; (f) K₂₀₀-Pt/L.

Table 3
Deconvoluted XPS data of the K_x-Pt/L samples.

Samples	Pt ^a /wt.%	K ^a /wt.%	Pt ⁰ composition ^b %	Pt ^{δ+} composition ^b /%	Pt ⁰ /Pt ^{δ+}
Pt/L	0.6	12.4	80.0	20.0	4.0
K ₅ -Pt/L	0.5	12.4	77.8	22.2	3.5
K ₂₀ -Pt/L	0.4	12.1	68.8	31.2	2.2
K ₈₀ -Pt/L	0.3	16.0	64.3	35.7	1.8
K ₂₀₀ -Pt/L	0.1	34.3	– ^c	– ^c	– ^c

^a Determined by EDS.

^b Determined by XPS.

^c Not determined.

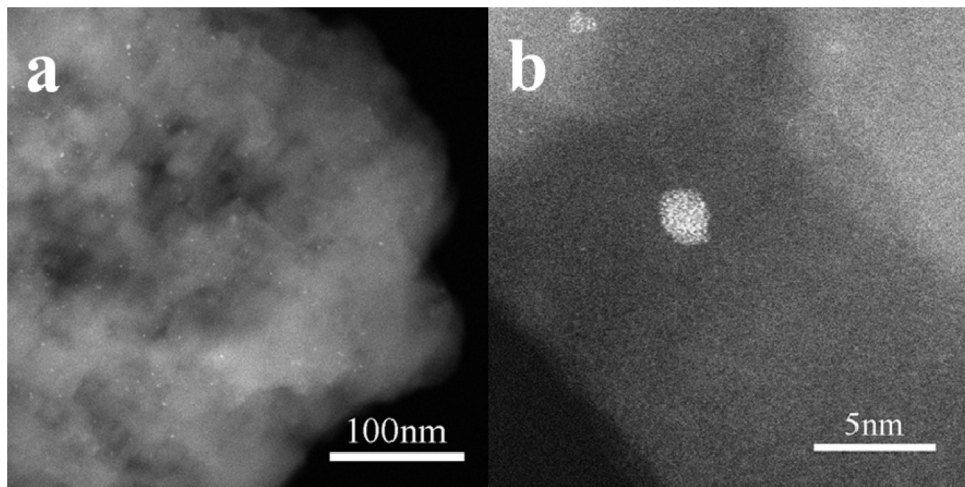


Fig. 5. Aberration-corrected transmission electron microscope images of K_{80} -Pt/L catalyst under the scale bar of (a) 100 nm and (b) 5 nm.

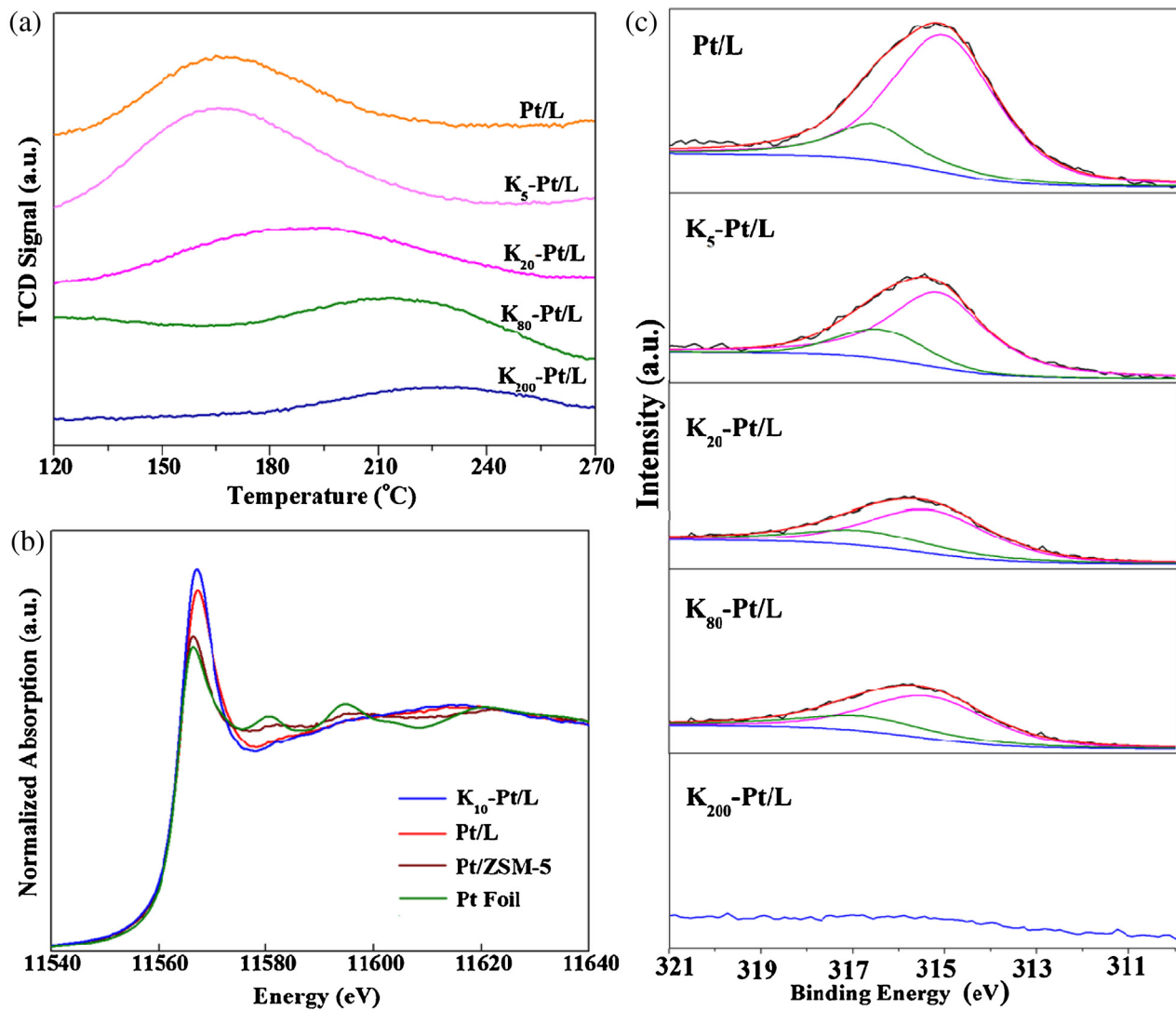


Fig. 6. (a) H_2 -TPR profiles of K_x -Pt/L catalysts; (b) Normalized XANES spectra at Pt LIII-edge of different Pt/zeolite catalysts after reduction at 500 °C; (c) The fitted Pt4d_{5/2} X-ray photoelectron spectra of K_x -Pt/L catalysts after reduction at 500 °C.

be classified based on the enthalpy values. Obviously, there were turning points on the adsorption heat curves for the K_x -Pt/L ($x=20, 80, 200$) samples, which illustrated the existence of two kinds of

adsorption sites. According to Virginie et al. [59], the enthalpy values in the high energetic stage were linked to the formation of carbonate species (denotes site I), while the low enthalpy values

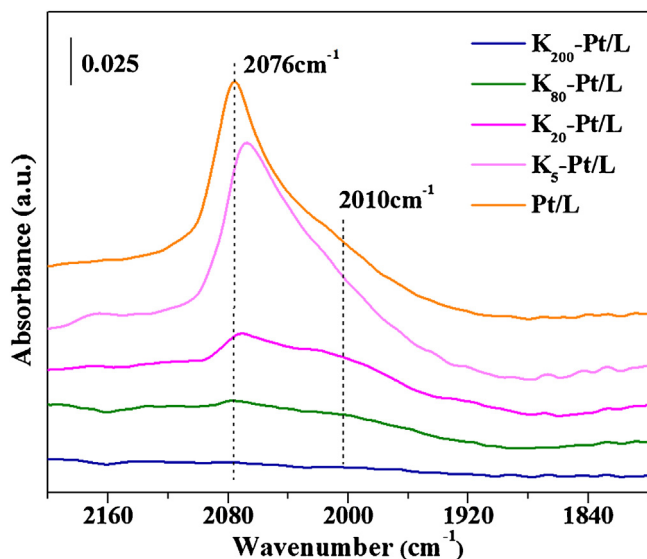
Fig. 7. FTIR spectra of adsorbed CO on K_x -Pt/L catalysts.

Table 4
Quantified microcalorimetry data over K_x -Pt/L catalysts.

Samples	CO ₂ adsorption / $\mu\text{mol g}^{-1}$			Initial heats / kJ mol^{-1}
	I	II	total	
Pt/L	0	11	11	92
K_5 -Pt/L	0	33	33	89.8
K_{20} -Pt/L	53	85	138	117.4
K_{80} -Pt/L	57	121	178	119.3
K_{200} -Pt/L	43	40	83	108.4

were associated with the formation of bicarbonate species (denotes site II).

On the basis of the enthalpy values, the content of the two kinds of adsorption species was quantified and recorded in Table 4. It was clear that, when the ratio of K/Pt was below 80, the adsorption amount of CO₂ on site II increased greatly with the increase of K loading, from 11 $\mu\text{mol L}^{-1}$ on Pt/L to 121 $\mu\text{mol L}^{-1}$ on K_{80} -Pt/L. That is to say, the additional K species stimulated the formation of bicarbonate species, which was easily formed by adsorption of CO₂ at the Pt-O(OH)-K interfaces. However, the formation of bicarbonate species was hindered over K_{200} -Pt/L, since the excessive amount of K overlaid the Pt particles and blocked the interface sites.

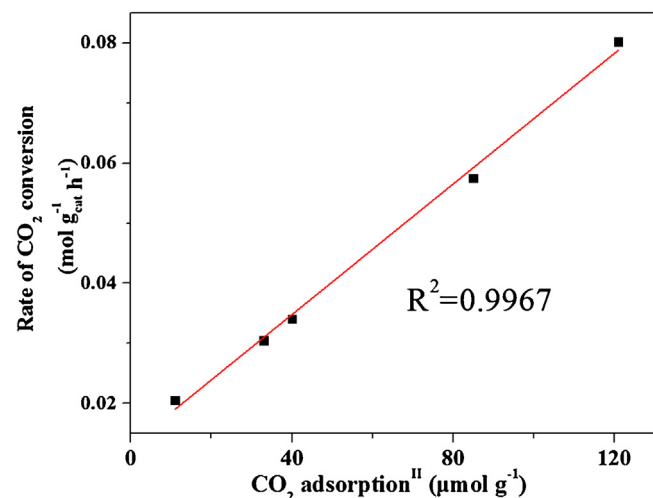
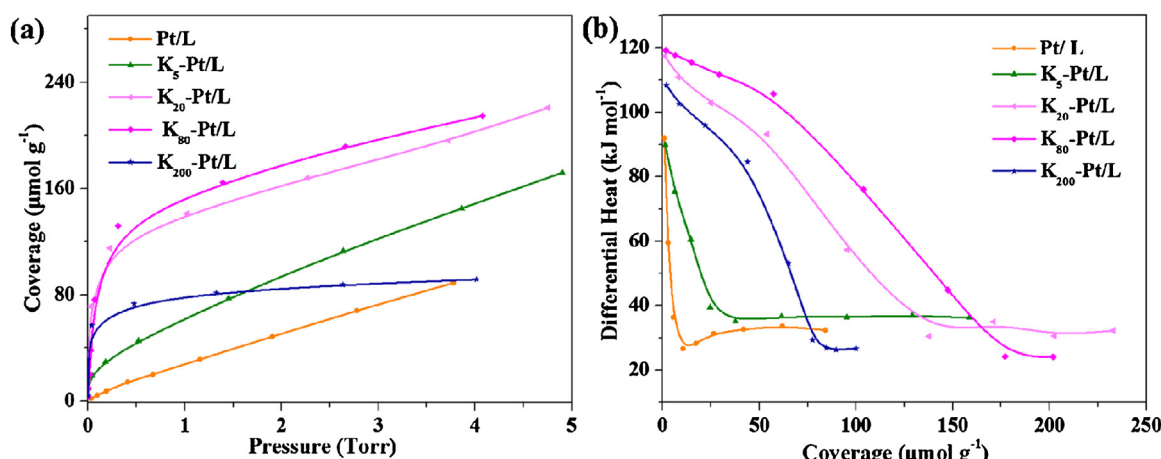


Fig. 9. The linear relationship diagram between the rate of CO₂ conversion ($\text{mol g}_{\text{cat}}^{-1} \text{h}^{-1}$) and the amount of adsorbed bicarbonate species. The reaction rates over the series K_x -Pt/L catalysts were calculated when reactions were conducted under 400 °C. Reaction rates collected under other reaction temperatures were also fitted with reasonable linear relationship, see Fig. S6.

Furthermore, in order to reveal the nature of active sites that promoted the activity and elucidate the structure-performance relationship, we correlated the amounts of adsorbed bicarbonate species on site II with the rates of CO₂ conversion. Surprisingly, there was a great linear relationship between the two parameters, as shown in Fig. 9. Thus, it was suggested that the surface bicarbonate was acted as active specie of the RWGS reaction which was easier formed at the interface sites between K promoters and platinum.

In-situ DRIFTS study was carried out over Pt/L and K_{20} -Pt/L catalysts to clarify the difference in the evolution of surface adsorbed species caused by extra addition of K promoter. Fig. 10(a) displays the signals obtained over Pt/L when it was exposed to the flowing of feed gas. At the very beginning, the intensity of two bands at 1640 cm^{-1} and 1668 cm^{-1} increased gradually, which were attributed to bidentate and monodentate formate species on potassium, respectively [60]. There was a surge appearance of a broad band at about 2000 cm^{-1} , showing that carbonyl species adsorbed quickly on Pt particles. However, there was a drastic change in the spectral features for K_{20} -Pt/L, as shown in Fig. 10(b). Firstly, the signals of adsorbed bidentate and monodentate formate species only appeared after 6 min with the purge of feed

Fig. 8. (a) Surface coverage and (b) differential heat of adsorption over K_x -Pt/L catalysts.

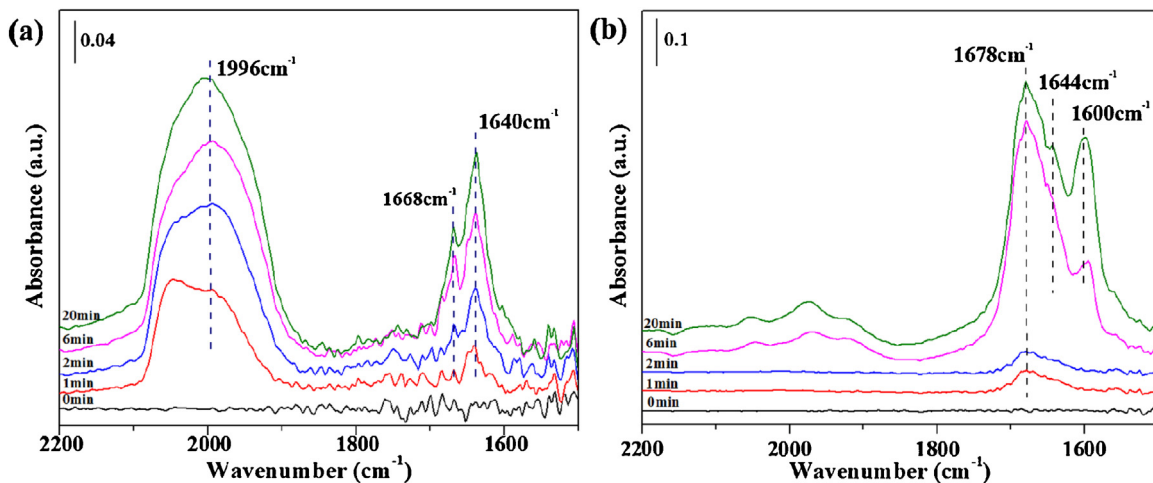
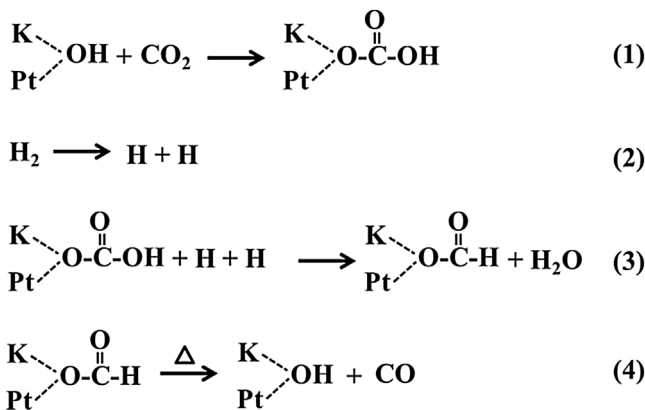


Fig. 10. *In-situ* DRIFT spectra collected over (a) Pt/L and (b) K₂₀-Pt/L catalysts. Measurements were conducted under 150 °C in a feed gas flow (50 ml min⁻¹).



Scheme 2. The reaction mechanism over K_x -Pt/L catalysts.

gas. After that, the peak intensity went through a sudden increase. Meanwhile, another prominent peak emerged at 1600 cm^{-1} with strong intensity. According to the statement previously [61], this new band can be ascribed to the bridge-bonded formate species at the interface site between platinum and K promoter, which solidly confirmed the formation of Pt-O(OH)-K interaction. Besides, the stretching region of metal-carbonyl species whose intensity was hardly observable showed a totally different situation, indicating the weakened interaction between CO and Pt particles [62].

Considering about the above phenomenon, the difference might be explained with the statement of Yang [29]. The original potassium ions in zeolite were functioned as a balance to the skeleton charge and mostly fixed at certain locations. Therefore, these kinds of potassium ions could hardly be used to cover or adjust the surface properties of platinum particles. However, with the addition by solid-state impregnation, K promoters may move through zeolite freely and distribute uniformly in zeolites, which was advantageous for the formation of Pt-O(OH)-K interaction. Obviously, the new interface sites greatly promoted the adsorption and activation of CO_2 , as well as the formation of formate intermediates. Moreover, the desorption of CO also became easier due to the existence of Pt-O(OH)-K interaction where the work function of Pt was increased via potassium promoter addition.

In summary of this section, with a set of *in-situ* DRIFTS and microcalorimetry experiments, the Pt-O(OH)-K interfaces were recognized as main active sites for RWGS reaction, where most of

surface bicarbonate species formed and further generated formate intermediates by hydrogenation. Overall, the reaction pathway was deduced as follows, shown in **Scheme 2**. Firstly, CO_2 adsorbed on the Pt-O(OH)-K interfaces or other potassium species and formed surface bicarbonate species, while H_2 homolytically dissociated on the adjacent platinum particles. The hydrogen atoms migrated and reacted with surface bicarbonate species to generate formate intermediates and water. Then, the formate intermediates further decomposed spontaneously and produced CO at the reaction temperature, higher than 200 $^{\circ}\text{C}$ [63]. During this process, the massive surface bicarbonate species forming at the Pt-O(OH)-K interfaces greatly accelerated the hydrogenation step, which was thought to be the key of the whole cycle. As a consequence, $\text{K}_x\text{-Pt/L}$ ($x \leq 80$) catalysts showed excellent performance in the RWGS reaction. However, the inaccessibility of Pt surfaces and interfaces with too much potassium addition increased the difficulty of H_2 and CO_2 activation, thus having a negative effect on the performance.

4. Conclusions

The present study shows a remarkable improvement in the catalytic performance of RWGS reaction over zeolite L supported platinum catalysts with the employment of extra K promoter. The approach toward “cage encapsulation” of metal particles in the L zeolite voids is indeed beneficial for the high dispersion and thermal stability of Pt particles, which contributes to the high selectivity of CO. In addition, the additive K promoters are favorable of forming an interaction with Pt particles through –O ligands, which not only alters the work function of platinum, but also formed Pt-O(OH)-K interface sites. With a set of *in-situ* DRIFTS and microcalorimetry characterizations, the Pt-O(OH)-K interface sites were identified as main active sites for RWGS reaction. The electronic properties of Pt-O(OH)-K sites, with a charge transfer from Pt surface to K, facilitated the formation of formate intermediates and CO desorption. However, with too much addition of K, the access of reactants to Pt surface and interfaces was blocked tightly. Thus, the RWGS activity was significantly promoted by the controlled addition of K promoter. This strategy for catalyst synthesis together with the detailed characterizations enable an emphasis on the critical role of promoters, as well as pave the way for a better understanding of RWGS reaction. In general, these insights provided a new option on how to design RWGS catalysts with high activity and selectivity, which might be also extended to other CO₂ hydrogenation reactions over supported noble metal catalysts.

Acknowledgements

The authors acknowledge the National Natural Science Foundation of China (Nos. 21476226, 21506204), China Ministry of Science and Technology under contract of 2016YFB0600902, Dalian Science Foundation for Distinguished Young Scholars (2016RJ04) and the Youth Innovation Promotion Association CAS for financial support. The authors also thank the BL14W at the Shanghai Synchrotron Radiation Facility for the XAS experiment.

Appendix A. Supplementary data

Supplementary data associated with this article can be found, in the online version, at <http://dx.doi.org/10.1016/j.apcatb.2017.05.067>.

References

- [1] A.R. Millward, O.M. Yaghi, *J. Am. Chem. Soc.* 127 (2005) 17998–17999.
- [2] H. Furukawa, O.M. Yaghi, *J. Am. Chem. Soc.* 131 (2009) 8875–8883.
- [3] H. Furukawa, N. Ko, Y.B. Go, N. Aratani, S.B. Choi, E. Choi, A.O. Yazaydin, R.Q. Snurr, M. O’Keeffe, J. Kim, O.M. Yaghi, *Science* 329 (2010) 424–428.
- [4] C.Á. Galván, J. Schumann, M. Behrens, J.L. García Fierro, R. Schlögl, E. Frei, *Appl. Catal. B* 195 (2016) 104–111.
- [5] I.A. Fisher, A.T. Bell, *J. Catal.* 162 (1996) 54–65.
- [6] J.H. Kwak, L. Kovarik, J. Szanyi, *ACS Catal.* 3 (2013) 2094–2100.
- [7] X.D. Xu, J.A. Moulijn, *Energy Fuels* 10 (1996) 305–325.
- [8] B.X. Hu, S. Frueh, H.F. Garces, L.C. Zhang, M. Aindow, C. Brooks, E. Kreidler, S.L. Suib, *Appl. Catal. B* 132 (2013) 54–61.
- [9] Y.A. Daza, J.N. Kuhn, *RSC Adv.* 6 (2016) 49675–49691.
- [10] J.C. Matsubu, S. Zhang, L. DeRita, N.S. Marinkovic, J.G. Chen, G.W. Graham, X. Pan, P. Christopher, *Nat. Chem.* 9 (2017) 120–127.
- [11] X. Chen, X. Su, B. Liang, X. Yang, X. Ren, H. Duan, Y. Huang, T. Zhang, *J. Energy Chem.* 25 (2016) 1051–1057.
- [12] X. Chen, X. Su, H. Duan, B. Liang, Y. Huang, T. Zhang, *Catal. Today* 281 (2016) 312–318.
- [13] M.D. Porosoff, S. Kattel, W. Li, P. Liu, J.G. Chen, *Chem. commun.* 51 (2015) 6988–6991.
- [14] X. Wang, H. Shi, J.H. Kwak, J. Szanyi, *ACS Catal.* 5 (2015) 6337–6349.
- [15] J.C. Matsubu, V.N. Yang, P. Christopher, *J. Am. Chem. Soc.* 137 (2015) 3076–3084.
- [16] R. Carrasquillo-Flores, I. Ro, M.D. Kumbhalkar, S. Burt, C.A. Carrero, A.C. Alba-Rubio, J.T. Miller, I. Hermans, G.W. Huber, J.A. Dumesic, *J. Am. Chem. Soc.* 137 (2015) 10317–10325.
- [17] M.D. Porosoff, X. Yang, J.A. Boscoboinik, J.G. Chen, *Angew. Chem.* 53 (2014) 6705–6709.
- [18] J. Schumann, M. Eichelbaum, T. Lunkenstein, N. Thomas, M.C. Alvarez Galvan, R. Schloegl, M. Behrens, *ACS Catal.* 5 (2015) 3260–3270.
- [19] D.H. Kim, J.L. Park, E.J. Park, Y.D. Kim, S. Uhm, *ACS Catal.* 4 (2014) 3117–3122.
- [20] M.D. Porosoff, J.G. Chen, *J. Catal.* 301 (2013) 30–37.
- [21] H.C. Wu, Y.C. Chang, J.H. Wu, J.H. Lin, I.K. Lin, C.S. Chen, *Catal. Sci. Technol.* 5 (2015) 4154–4163.
- [22] J.C. Matsubu, V.N. Yang, P. Christopher, *J. Am. Chem. Soc.* 137 (2015) 3076–3084.
- [23] I.V. Yentekakis, G. Goula, P. Panagiotopoulou, S. Kampouri, M.J. Taylor, G. Kyriakou, R.M. Lambert, *Appl. Catal. B* 192 (2016) 357–364.
- [24] M. Yang, S. Li, Y. Wang, J.A. Herron, Y. Xu, L.F. Allard, S. Lee, J. Huang, M. Mavrikakis, M. Flytzani-Stephanopoulos, *Science* 346 (2014) 1498–1501.
- [25] B. Zugic, S. Zhang, D.C. Bell, F. Tao, M. Flytzani-Stephanopoulos, *J. Am. Chem. Soc.* 136 (2014) 3238–3245.
- [26] B. Zugic, D.C. Bell, M. Flytzani-Stephanopoulos, *Appl. Catal. B* 144 (2014) 243–251.
- [27] R. Carrasquillo-Flores, I. Ro, M.D. Kumbhalkar, S. Burt, C.A. Carrero, A.C. Alba-Rubio, J.T. Miller, I. Hermans, G.W. Huber, J.A. Dumesic, *J. Am. Chem. Soc.* 137 (2015) 10317–10325.
- [28] R.M. Levy, D.J. Bauer, *J. Catal.* 9 (1967) 76–86.
- [29] Y. Zhai, D. Pierre, R. Si, W. Deng, P. Ferrin, A.U. Nilekar, G. Peng, J.A. Herron, D.C. Bell, H. Saltzburg, M. Mavrikakis, M. Flytzani-Stephanopoulos, *Science* 329 (2010) 1633–1636.
- [30] J.D. Kistler, N. Chotigkrai, P.H. Xu, B. Enderle, P. Praserthdam, C.Y. Chen, N.D. Browning, B.C. Gates, *Angew. Chem.* 53 (2014) 8904–8907.
- [31] G. Avgouropoulos, E. Oikonomopoulos, D. Kanistras, T. Ioannides, *Appl. Catal. B* 65 (2006) 62–69.
- [32] F. Ghoroghchian, H. Aghabozorg, F. Farhadi, H. Kazemian, *Chem. Eng. Technol.* 33 (2010) 2066–2072.
- [33] H. Kivrak, Á. Mastalir, Z. Király, D. Uneret, *Catal. commun.* 10 (2009) 1002–1005.
- [34] Y. Jun-ying, W.E. Swartz, *Spectrosc. Lett.* 17 (2006) 331–343.
- [35] S.S. Kim, H.H. Lee, S.C. Hong, *Appl. Catal. B* 119 (2012) 100–108.
- [36] S.S. Kim, K.H. Park, S.C. Hong, *Fuel Process. Technol.* 108 (2013) 47–54.
- [37] A. Bansode, B. Tidona, P.R. von Rohr, A. Urakawa, *Catal. Sci. Technol.* 3 (2013) 767–778.
- [38] J.H. Kwak, L. Kovarik, J. Szanyi, *ACS Catal.* 3 (2013) 2094–2100.
- [39] J.H. Kwak, L. Kovarik, J. Szanyi, *ACS Catal.* 3 (2013) 2449–2455.
- [40] Z. Wu, S. Goel, M. Choi, E. Iglesia, *J. Catal.* 311 (2014) 458–468.
- [41] X. Yang, X. Su, X. Yang, Y. Huang, A. Wang, T. Zhang, *CIESC J.* 67 (2016) 73–82.
- [42] M. Yang, J. Liu, S. Lee, B. Zugic, J. Huang, L.F. Allard, M. Flytzani-Stephanopoulos, *J. Am. Chem. Soc.* 137 (2015) 3470–3473.
- [43] Z. Yuan, P. Wu, J. Gao, X. Lu, Z. Hou, X. Zheng, *Catal. Lett.* 130 (2009) 261–265.
- [44] C. Yu, Q. Ge, H. Xu, W. Li, *Appl. Catal. A* 315 (2006) 58–67.
- [45] L. Wang, H. Chen, M.-H. Yuan, S. Rivillon, E.H. Klingenber, J.X. Li, R.T. Yang, *Appl. Catal. B* 152–153 (2014) 162–171.
- [46] X. Zhu, M. Shen, L.L. Lobban, R.G. Mallinson, *J. Catal.* 278 (2011) 123–132.
- [47] B. Liang, H. Duan, X. Su, X. Chen, Y. Huang, X. Chen, J.J. Delgado, T. Zhang, *Catal. Today* 281 (2017) 319–326.
- [48] J.Z. Shyu, K. Otto, *Appl. Surf. Sci.* 32 (1988) 246–252.
- [49] A. Bourane, O. Dulaurent, D. Bianchi, *Langmuir* 17 (2001) 5496–5502.
- [50] K.C. Petallidou, A.M. Efstathiou, *Appl. Catal. B* 140 (2013) 333–347.
- [51] P. Angevaare, H. Hendrickx, V. Ponec, *J. Catal.* 110 (1988) 11–17.
- [52] C.S. Chen, W.H. Cheng, S.S. Lin, *Appl. Catal. A* 238 (2003) 55–67.
- [53] G.J. Millar, C.H. Rochester, K.C. Waugh, *J. Catal.* 155 (1995) 52–58.
- [54] J. Nicole, D. Tsiplakides, C. Pliangos, X.E. Verykios, Ch. Comminellis, C.G. Vayenas, *J. Catal.* 204 (2001) 23–34.
- [55] P. Vernoux, F. Sapountzi, M.N. Tsampas, L. Lizarraga, A. De Lucas-Consuegra, J.L. Valverde, S. Soutentie, C.G. Vayenas, D. Tsiplakides, E. Baranova, *Chem. Rev.* 113 (2013) 8192–8260.
- [56] A. Maroto, I. Rodriguez-Ramos, A. Guerrero-Ruiz, J. Llorca, P.R. de la Piscina, N. Homs, *Appl. Organomet. Chem.* 14 (2000) 783–788.
- [57] S.V. Bordawekar, R.J. Davis, *J. Catal.* 189 (2000) 79–90.
- [58] L. He, Q. Lin, Y. Liu, Y. Huang, J. Enerny, *Chem.* 23 (2014) 587–592.
- [59] V. Hornebecq, C. Knöfel, P. Boulet, B. Kuchta, P.L. Llewellyn, *J. Phys. Chem. C* 115 (2011) 10097–10103.
- [60] A. Hagofer, D. Ferri, K. Foettinger, G. Rupprechter, *ACS Catal.* 2 (2012) 2305–2315.
- [61] G.J. Millar, C.H. Rochester, K.C. Waugh, *J. Catal.* 142 (1993) 263–273.
- [62] M. Kuriyama, H. Tanaka, S. Ito, T. Kubota, T. Miyao, S. Naito, K. Tomishige, K. Kunimori, *J. Catal.* 252 (2007) 39–48.
- [63] J. Quan, T. Kondo, G. Wang, J. Nakamura, *Angew. Chem.* 56 (2017) 1–6.